



# Benefits and limitations of Pt nanoparticles supported on highly porous antimony-doped tin dioxide aerogel as alternative cathode material for proton-exchange membrane fuel cells



Gwenn Cognard<sup>a,b,\*</sup>, Guillaume Ozouf<sup>c</sup>, Christian Beauger<sup>c</sup>, Grégory Berthomé<sup>d,e</sup>, David Riassetto<sup>f,g</sup>, Laetitia Dubau<sup>a,b</sup>, Raphaël Chattot<sup>a,b</sup>, Marian Chatenet<sup>a,b,h</sup>, Frédéric Maillard<sup>a,b,\*</sup>

<sup>a</sup> Univ. Grenoble Alpes, LEPMI, F-38000 Grenoble, France

<sup>b</sup> CNRS, LEPMI, F-38000 Grenoble, France

<sup>c</sup> MINES ParisTech, PSL Research University PERSEE—Centre procédés, énergies renouvelables et systèmes énergétiques, CS 10207 rue Claude Daunesse, F-06904 Sophia Antipolis Cedex, France

<sup>d</sup> Univ. Grenoble Alpes, SIMaP, F-38000 Grenoble, France

<sup>e</sup> CNRS, SIMaP, F-38000 Grenoble, France

<sup>f</sup> Univ. Grenoble Alpes, LMGP, F-38000 Grenoble, France

<sup>g</sup> CNRS, LMGP, F-38000 Grenoble, France

<sup>h</sup> French University Institute, Paris, France

## ARTICLE INFO

### Article history:

Received 17 May 2016

Received in revised form 28 July 2016

Accepted 3 August 2016

Available online 4 August 2016

### Keywords:

Antimony-doped tin dioxide (Sb-doped SnO<sub>2</sub>, ATO)

Platinum nanoparticles

Aerogel

Oxygen reduction reaction (ORR)

Proton exchange membrane fuel cell (PEMFC)

## ABSTRACT

An electron-conducting metal-oxide substrate must fulfill three criteria to represent a viable alternative to conventional carbon blacks used as supports for Pt-based nanoparticles in proton-exchange membrane fuel cell (PEMFC): (i) be electron-conducting, (ii) be corrosion resistant and (iii) possess an opened porous structure compatible with facile ionomer insertion and efficient mass-transport properties. Using a sol-gel route, antimony-doped tin dioxide (Sb-doped SnO<sub>2</sub>, ATO) aerogels with such characteristics were synthesized: an optimal Sb content of 10 at.% was found in terms of specific surface area and electrical conductivity. Pt nanoparticles were loaded onto 10 at.% Sb-doped SnO<sub>2</sub> (Pt/ATO), undoped SnO<sub>2</sub> (Pt/SnO<sub>2</sub>) and Vulcan XC72 (Pt/C) via a modified polyol route, and their electrocatalytic activity for the oxygen reduction reaction (ORR) was evaluated. A 2-fold enhancement in ORR specific activity was measured on Pt/ATO over Pt/C. An accelerated stress test (AST) protocol, mimicking start-up/shutdown events in a PEMFC, was used to determine the long-term ORR performance of the Pt/ATO and the reference Pt/C electrocatalysts. The carbon support was not robust enough in these harsh conditions, as observed from the massive detachment of Pt nanoparticles from Vulcan XC72. On the contrary, the Pt nanoparticles did not detach from the ATO support. However, a core@shell structure with a Sb-poor surface covering a core featuring a Sb content close to the nominal formed during the AST. This core@shell structure restricted the capacity of the Pt nanoparticles to exchange electrons, as evidenced by the attenuated Pt surface oxide formation/reduction features, and led to decreased catalytic activity for the ORR.

© 2016 Elsevier B.V. All rights reserved.

## 1. Introduction

Proton Exchange Membrane Fuel Cells (PEMFC) are high-efficiency energy converters that can be deployed for mobile, transport and stationary applications in an eco-friendly man-

ner. Nevertheless, their large-scale development requires further improvements, specifically regarding their lifetime in operation [1]. Indeed, the harsh operating conditions of a PEMFC cathode (high electrochemical potential, presence of oxygen and water, acidic pH, formation of radical species) strongly degrade the carbon-supported platinum or platinum-alloy nanoparticles (Pt/C or Pt-alloy/C, respectively) used to catalyze the electrochemical reactions, and depreciate the overall PEMFC performances. The Pt/C or Pt-alloy/C materials degradation proceeds via (i) dissolution of the metal/alloy nanocrystallites (electrochemical Ostwald

\* Corresponding authors at: CNRS, LEPMI, F-38000 Grenoble, France.

E-mail addresses: [gwenn.cognard@grenoble-inp.org](mailto:gwenn.cognard@grenoble-inp.org) (G. Cognard), [frederic.maillard@lepmi.grenoble-inp.fr](mailto:frederic.maillard@lepmi.grenoble-inp.fr) (F. Maillard).

ripening) [2], (ii) reduction of the  $\text{Pt}^{z+}$  ions produced by electrochemical Ostwald ripening into the proton-exchange membrane or the ionomer contained in the electrodes [3–5], (iii) migration, aggregation and coalescence of the metal nanocrystallites [6], and (iv) corrosion of the carbon support (carbon oxidation reaction—COR) [7,8].

The COR is thermodynamically possible at potentials above 0.2 V vs. the reversible hydrogen electrode (RHE) [9] but kinetically limited up to 0.9 V vs. RHE; therefore it is essentially a concern at the cathode [7,8,10–13]. This reaction proceeds faster on disordered domains of the carbon support (amorphous carbon and defective graphite crystallites), a phenomenon that facilitates the detachment of Pt or Pt-alloy nanoparticles [7,8,14]. The COR kinetics is also strongly accelerated under abnormal PEMFC operating conditions, such as localized fuel starvation [15,16] or start-up/shutdown events [17–19], where the positive electrode potential may reach as high as 1.5–1.6 V vs. RHE. Excursions to high electrode potential values cause extensive carbon corrosion and collapse of the electrode structure within a few seconds [20], therefore yielding considerable mass-transport losses (“asphyxiation” of the active sites which are starved from oxygen). To tackle this problem, “system solutions” and “materials solutions” are currently implemented. Possible system solutions involve using an external load during gas purges [21] or purging the anode with an inert gas when the PEMFC system is stopped. Examples of materials solutions are to use highly-graphitic carbons supports [8,22] or carbon-free catalyst supports based on metal oxides [23–38].

Replacing conventional carbon supports by metal oxides implies that the latter fulfill at least three criteria of equal relevance: (i) be electron-conducting and (ii) corrosion-resistant, and (iii) possess an opened and interconnected structure compatible with facile gas/water transport and ionomer insertion. To date, only  $\text{TiO}_2$ ,  $\text{Nb}_2\text{O}_3$ ,  $\text{MoO}_3$ ,  $\text{SnO}_2$  and  $\text{Ta}_2\text{O}_5$  fulfill the stability (corrosion-resistance) criterion [9,38,39]. Moreover, since most of the metal oxides are semiconductors, doping with hypovalent or hypervalent ions or using composite electrodes based on metal oxide and carbon is a pre-requisite to high electron conductivity [31,37–41]. The optimal doping content depends on the chemical nature of the ions, on the structure (crystal structure, crystallite size) and on the morphology (plate, sphere, tube, fiber) of the metal oxide, and must be carefully adjusted [24,42]. Yet importantly, large specific surface-area is required to enable high dispersion of the Pt nanoparticles and allow efficient mass-transport of reactants to (and products from) the electrode. Therefore, a proper balance must be found between small mesopores (dispersion of the Pt phase), large mesopores and macropores (efficient mass-transport). The combination of corrosion resistance, electrical conductivity and porosity criteria in the same nanomaterial is highly challenging.

Tin oxide ( $\text{SnO}_2$ ) is one of the most investigated metal oxide, with application as a solid-state gas sensor material, oxidation catalyst, and transparent conductor [41]. It is also a promising support at PEMFC cathode when doped with Nb, Sb, Ta or Ru [38–40,43]. Indeed, *n*-type dopants increase the free-electron concentration, and upshift the Fermi level near the conduction band of  $\text{SnO}_2$  [44], thereby heightening its electrical conductivity. However, despite their crucial fundamental and applied importance, studies on the long-term stability of the doping element in PEMFC operating conditions remain scarce. Kakinuma, Senoo *et al.* [31,40] showed that Ta-doped  $\text{SnO}_2$ , Nb-doped  $\text{SnO}_2$  and Sb-doped  $\text{SnO}_2$  release Sn atoms (<0.02 at.%) but no dopant when they are immersed for  $t = 1000$  h in 0.1 M  $\text{H}_2\text{SO}_4$  at  $T = 353$  K under reducing conditions ( $\text{H}_2$  bubbling). In contrast, Fabbri *et al.* [27] detected a loss of Sb atoms from Sb-doped  $\text{SnO}_2$  after an accelerated stress test (AST) composed of 1,000 potential cycles between 0.5 and 1.5 V vs. RHE in  $\text{O}_2$ -saturated electrolyte. This was rationalized by considering

that Sb atoms segregate to the  $\text{SnO}_2$  surface, and dissolve into the electrolyte.

In this study, ATO aerogels were synthesized by sol-gel route in acidic media using metal alkoxide precursors and drying under  $\text{CO}_2$  in supercritical conditions. This method allowed tuning their specific surface area, pore size distribution, and the degree of doping with Sb. Using specific surface area and electrical conductivity as cutoff criteria, a Sb content of 10 at.% revealed optimal. Pt nanoparticles were loaded onto 10% Sb-doped  $\text{SnO}_2$  support via a modified polyol synthesis and their electrocatalytic activity for the ORR was tested in liquid electrolyte at  $T = 330$  K, and compared to that of two reference materials derived from the same Pt colloidal solution: Pt/C and Pt/ $\text{SnO}_2$  (undoped). The structural and chemical changes of the Pt/ATO and the reference Pt/C electrocatalysts during the AST were monitored by scanning electron microscopy (SEM), transmission electron microscopy (TEM), high-angle annular dark-field imaging in scanning transmission electron microscopy mode (HAADF-STEM), X-ray energy-dispersive spectroscopy (X-EDS) and X-ray photoelectron spectroscopy (XPS).

## 2. Experimental

### 2.1. Synthesis of the ATO supports

ATO aerogels were synthesized by sol-gel route, using metal alkoxide precursors. A solution containing nitric acid ( $\text{HNO}_3$ , Alfa Aesar, 2N), water and isopropanol (Acros Organics, 99.5%) was slowly dripped under magnetic stirring into a solution of tin isopropoxide ( $\text{Sn(IV)}$  isopropoxide, Alfa Aesar) in isopropanol (iPrOH) with a corresponding amount of dopant precursor (Sb(III) isopropoxide, Alfa Aesar). Using  $\text{HNO}_3/\text{Sn} = 0.072$ ,  $\text{H}_2\text{O}/\text{Sn} = 3.06$ , and  $\text{iPrOH}/\text{Sn} = 119$  molar ratios, a gel formed after few minutes. To prevent drying, the gel was covered with isopropanol, and left as is during  $t = 48$  h for aging. After washing (three times a day for two days), the gels were dried under  $\text{CO}_2$  in supercritical conditions ( $P = 80$  bar,  $T = 313$  K) to get aerogels. The resulting materials were heat treated under air at  $T = 873$  K during  $t = 5$  h. After this calcination step, the color of the samples turned blue.

### 2.2. Deposition of Pt nanoparticles

Two synthesis routes were used to deposit Pt nanoparticles onto the ATO support (the optimal Pt mass fraction being 20 wt.%, see Fig. S1): photoreduction or chemical reduction via a modified polyol method. In both methods, a colloidal solution of Pt nanoparticles was first synthesized. For the photoreduction, 34 mg of  $\text{H}_2\text{PtCl}_6 \cdot 6\text{H}_2\text{O}$  (dihydrogen hexachloroplatinate (IV) hexahydrate, 99.9%, Alfa Aesar) were dissolved in a water:ethanol (80:20 vol.) solution following the procedure previously described in Ref. [45]. The solution was then exposed to ultra-violet (UV) light using three UVA lamps (PLS 11W from Philips), essentially emitting at a 365 nm wavelength, for  $t = 12$  h in a climatic chamber regulated at  $T = 293$  K and 40% relative humidity. For the polyol method, 34 mg of  $\text{H}_2\text{PtCl}_6 \cdot 6\text{H}_2\text{O}$  were dissolved in 60 mL of ethylene glycol (Rotipuran®, Roth). The pH was then adjusted to 11.5 using sodium hydroxide (Suprapur®, Merck), the solution was purged with argon (99.99%, Messer) and heated at  $T = 433$  K for  $t = 3$  h. 50 mg of the desired support—ATO, pure  $\text{SnO}_2$  or Vulcan XC72—was then mixed to the colloidal solution and the pH was adjusted to 2 using sulfuric acid (Suprapur®, Merck). It was stirred for  $t = 12$  h, then filtered with a 0.22  $\mu\text{m}$  membrane filter (Durapore® membrane filters, polyvinylidene fluoride), and thoroughly rinsed with ultrapure water. Finally, the samples were heat-treated for  $t = 2$  h at  $T = 333$  K in air.

### 2.3. Electrochemical characterizations in liquid electrolyte

All the glassware used in this study was cleaned by  $t > 12$  h immersion in a  $\text{H}_2\text{SO}_4/\text{H}_2\text{O}_2$  mixture and thoroughly rinsed with MQ-grade water (18.2 M $\Omega$  cm, 1–3 ppm TOC) before use. The electrolyte (0.1 M  $\text{H}_2\text{SO}_4$ ) was prepared from MQ-grade water and  $\text{H}_2\text{SO}_4$  (Suprapur<sup>®</sup>, Merck). The electrochemical characterization of the catalytic materials and the AST were conducted in two separated four-electrode electrochemical glass cells, a characterization and a degradation cell, both thermostated at  $T = 330$  K. As shown recently by Dubau *et al.* [46] performing the AST at  $T = 330$  K more accurately reflects the changes in morphology and surface reactivity occurring in real PEMFC environment, and provides gain in time. The counter-electrode was a glassy carbon plate (to avoid contamination of the working electrode by metal cations resulting from its dissolution), and the reference electrode a mercury sulfate electrode (MSE,  $\text{Hg}|\text{Hg}_2\text{SO}_4|\text{saturated K}_2\text{SO}_4$ ) was connected to the cell via a Luggin capillary. The reference-electrode was calibrated periodically by measuring its potential difference with a RHE, which was systematically 0.72 V vs. RHE. A Pt wire connected to the reference-electrode was used to filter the high frequency electrical noise and to avoid disturbing the low frequency electrical measurements. The working electrode (WE) was a rotating disk electrode (RDE) made of glassy carbon (Sigradur<sup>®</sup>, 0.196 cm<sup>2</sup>) onto which an aliquot of an ink containing the studied electrocatalyst (Pt/ATO or Pt/C) was drop-casted and dried in air at  $T = 383$  K. The ink was composed of 5 wt.% Nafion<sup>®</sup> perfluorinated-sulfonic acid solution (Aldrich), MQ-grade water and the electrocatalyst (Pt concentration of 0.147 g<sub>Pt</sub> L<sup>-1</sup>). The suspension was ultrasonically treated during at least 15 min. Depending on the aliquot volume, the Pt loading was varied between 10 and 120  $\mu\text{g}_{\text{Pt}} \text{cm}_{\text{geo}}^{-2}$ . A Pt loading of  $L_{\text{Pt}} = 60 \mu\text{g}_{\text{Pt}} \text{cm}_{\text{geo}}^{-2}$  (Fig. S2) was found optimal in terms of Pt specific surface area, specific activity for the ORR and durability viewpoints (the specific ORR activity should be measurable after the AST).

The electrochemical characterizations were performed with an Autolab potentiostat (PGSTAT 302N). The WE was first immersed in the argon-purged electrolyte at controlled potential  $E = 0.40$  V vs. RHE and 15 cyclic voltammograms (CVs) were recorded at  $\nu = 0.1 \text{ V s}^{-1}$  between 0.05 and 1.23 V vs. RHE. The electrolyte was then saturated with  $\text{O}_2$  and 5 linear sweep voltammograms with Ohmic drop compensation were recorded at  $\nu = 0.005 \text{ V s}^{-1}$  between 0.40 and 1.05 V vs. RHE. Finally, the electrolyte was purged with argon and 15 CVs with Ohmic drop compensation were recorded at  $\nu = 0.1 \text{ V s}^{-1}$  in the range  $0.05 < E < 1.23$  V vs. RHE. The coulometry required to adsorb and desorb under-potentially deposited hydrogen ( $\text{H}_{\text{upd}}$ ) was used to determine the electrochemically active surface area (ECSA) assuming a charge density of 210  $\mu\text{C cm}^{-2}$  of Pt. The ECSA was determined on the 15<sup>th</sup> cycle following ORR measurements for both fresh/aged samples. We tested two baseline correction methods: (i) measuring the CV of the Pt-free  $\text{SnO}_2$  or ATO support and subtracting the measured pseudo-capacitive current to that measured the Pt/ $\text{SnO}_2$  or Pt/ATO, (ii) a simple straight line between 0.40 and 0.05 V vs. RHE was also tested. No difference was observed between the two approaches, and hence the straight baseline correction between 0.40 and 0.05 V vs. RHE was adopted.

### 2.4. Accelerated stress test

To investigate the effect of startup/shutdown or fuel starvation events, AST protocols from the Fuel Cell Commercialization Conference of Japan (FCCJ) were used [47]. The electrode potential was modulated with a square wave between 1.0 and 1.5 V vs. RHE with a holding time of 3 s at each voltage. 5,000 or 10,000 cycles were performed in the degradation electrochemical cell. To avoid

the effect of intermediate characterizations, [48] independent electrodes were used for each AST (i.e. the 5,000th and the 10,000th cycles are obtained with different electrodes).

### 2.5. Atomic absorption spectrometry

The Pt content of each electrocatalyst was measured by atomic absorption spectrometry on a PinAAcle 900F (PerkinElmer) spectrometer. A 5 mg portion of the Pt/ATO or the Pt/C electrocatalyst was firstly digested in concentrated aqua regia (3:1 HCl:HNO<sub>3</sub> by volume) made from high purity acids (Suprapur<sup>®</sup>, Merck) at  $T = 333$  K for  $t = 12$  h. The obtained solution was then pipetted and diluted in MQ-grade water until a known volume (10 mL).

### 2.6. Transmission electron microscopy imaging

The fresh/aged catalytic layers were scratched from the glassy carbon, dispersed in MQ-grade water and deposited onto a copper grid (200 mesh, Lacey formvar/carbon, Ted Pella) for TEM observations. The Pt particle size distribution was obtained from TEM or X-EDS elemental maps images by counting only the isolated particles. The surface-averaged mean particle size  $d_s$  and the volume-averaged mean particle size  $d_v$  were then determined using the following equations:

$$d_s = \frac{\sum_i n_i d_i^3}{\sum_i n_i d_i^2} \quad (1)$$

$$d_v = \frac{\sum_i n_i d_i^4}{\sum_i n_i d_i^3} \quad (2)$$

HAADF-STEM images and X-EDS elemental maps of the Pt/ATO electrocatalysts were acquired using a JEOL 2100F microscope operated at 200 kV in STEM mode, and equipped with a retractable SDD Centurio detector. The X-EDS spectra were recorded on individual Pt/ATO particles by scanning the beam in a square region adjusted to the ATO particle size. The quantitative analyses were performed on the Pt M and the Sn L lines using the  $K$ -factor provided by the JEOL software. Note that it was not possible to distinguish Sb atoms from Sn atoms in X-EDS elemental maps because the Sn L and Sb L emission overlap (3.44 and 3.60 keV, respectively). The fresh and the aged Pt/C electrocatalysts were examined with a Jeol 2010 TEM operated at 200 kV with a point-to-point resolution of 0.19 nm. The average Sb/(Sn + Sb) ratio was determined by X-EDS on fifteen individual zones.

### 2.7. X-ray diffraction measurements

The different supports were analyzed using an PANalytical X'Pert pro Philips diffractometer operated at 45 kV and 30 mA and Cu K $\alpha$  radiation ( $\lambda = 0.15418$  nm). The data were collected in steps of  $0.05^\circ$  from  $20^\circ$  to  $90^\circ$  in  $2\theta$  mode. The synthesized electrocatalysts were analyzed using a PANalytical X'Pert Pro MPD vertical goniometer/diffractometer operating at 45 kV and 40 mA using Cu K $\alpha$  radiation and a diffracted-beam monochromator. The  $2\theta$  angle extended from  $15^\circ$  to  $139^\circ$  and varied using a step size of  $0.067^\circ$  accumulating data for 320 s. To avoid interferences with other peaks originating from the ATO support, the Pt crystallite size was determined from the (111) diffraction peak at  $2\theta = 39.8^\circ$  using the Debye-Scherrer equation.

### 2.8. X-ray photoelectron spectroscopy

The XPS surveys were obtained on a XR3E2 spectrometer (Vacuum Generator) equipped with a Mg K $\alpha$  (1253.6 eV) X-ray source powered at 300 W (15 kV–20 mA). To correct for any charging

effect, all the binding energies were referenced to the graphene component of the carbon C1s peak at 284.6 eV. Since the  $\text{Sb}3\text{d}_{5/2}$  peak overlaps with the O1s signal, the  $\text{Sn}3\text{d}_{5/2}$  and  $\text{Sb}3\text{d}_{3/2}$  peaks were integrated to determine the quantity of Sn and Sb (see Fig. S3). A ratio of 2/3 between the areas of the  $\text{Sb}3\text{d}_{5/2}$  and  $\text{Sb}3\text{d}_{3/2}$  peaks was assumed [49] and the experimental values of the relative sensitivity factors (RSF) were determined for  $\text{Sn}3\text{d}_{5/2}$  and  $\text{Sb}3\text{d}_{5/2}$  and compared to theoretical ones [50]. According to Eq. (3), the experimental RSFs values for an element  $i$  equal:

$$\text{RSF}_i = T_i \cdot \lambda_i \cdot \sigma_i \quad (3)$$

where  $T_i$  is the transmission factor,  $\lambda_i$  the inelastic mean free path (IMFP) and  $\sigma_i$  the photoionization cross section. The  $T_i$  term for the device used in this study was estimated in former work (Eq. (4)) [51]:

$$T_i = \left( \frac{1}{E_{ki}} \right)^{0.7} \quad (4)$$

$\lambda_i$  was calculated from the TPP-2M formula [52] and Scofield values [53] were used for  $\sigma_i$ . According to Eq. (5), the  $\text{Sb}/(\text{Sb} + \text{Sn})$  ratio depends on the ratio  $r = \frac{\text{RSF}_{\text{Sb}}}{\text{RSF}_{\text{Sn}}}$ . The experimental ratio  $r_{\text{exp}}$  was found close to  $r_{\text{exp}} = 1.3$ , and the theoretical ratio  $r_{\text{th}} = 1.1$  [50].

$$\frac{\text{Sb}}{\text{Sb} + \text{Sn}} = \frac{\frac{I_{\text{Sb}}}{\text{RSF}_{\text{Sb}}}}{\frac{I_{\text{Sb}}}{\text{RSF}_{\text{Sb}}} + \frac{I_{\text{Sn}}}{\text{RSF}_{\text{Sn}}}} = \frac{I_{\text{Sb}}}{I_{\text{Sb}} + I_{\text{Sn}} \cdot \frac{\text{RSF}_{\text{Sb}}}{\text{RSF}_{\text{Sn}}}} \quad (5)$$

To evaluate the near surface composition and the bulk composition of the fresh metal oxide supports, the  $\text{Sb}/(\text{Sb} + \text{Sn})$  ratio determined by XPS was compared to that measured by X-EDS, respectively.

### 2.9. Electrical conductivity measurements

The electrical conductivity of the ATO aerogels was investigated by direct resistance measurements in a homemade conductivity cell, made up of two copper electrodes ( $S = 0.785 \text{ cm}^2$ ). The samples were positioned between these two electrodes, a current of 105, –105, or 400 mA was applied, and the voltage measured for each current. The electrical conductivity measurements were made in a press at room temperature, with pressures of 0,  $6.5 \times 10^2$  and  $13 \times 10^2 \text{ kg cm}^{-2}$ . The electrical conductivity ( $\sigma$ ) reported in Table 1 was calculated with the formula:

$$\sigma = e/(R \times S_{\text{electrode}}) \quad (6)$$

where  $e$  is the thickness of the sample,  $R$  the measured resistance, and  $S_{\text{electrode}}$  the surface of the electrode at a pressure of 50 kPa.

## 3. Results and discussion

### 3.1. Preparation and characterization of the Sb-doped $\text{SnO}_2$ supports

ATO supports with different degrees of doping with Sb (5, 10 and 15 at.%) were firstly synthesized by sol-gel route in acidic media using metal alkoxide precursors, namely  $\text{Sn}(\text{IV})$  isopropoxide and  $\text{Sb}(\text{III})$  isopropoxide. As shown by Table 1, doping  $\text{SnO}_2$  by Sb impressively increased the electrical conductivity: the electronic conductivity of the pure  $\text{SnO}_2$  and 10 at.% Sb-doped  $\text{SnO}_2$  aerogels at room temperature and under a pressure of  $P = 50 \text{ kPa}$  were  $2 \times 10^{-5} \text{ S cm}^{-1}$  and  $0.13 \text{ S cm}^{-1}$ , respectively. However, the variation in electrical conductivity was nonlinear with the doping level. This may be explained by considering segregation of Sb atoms to the surface in ATO. Indeed, at low doping levels, some  $\text{Sn}^{4+}$  ions are substituted by  $\text{Sb}^{5+}$  ions, resulting in more conduction electrons, and thus increased electrical conductivity. However, as described

in the literature [54–58], should the doping level exceed 4–5 at.%, the  $\text{Sb}^{5+}$  ions segregate to the surface where they are reduced into  $\text{Sb}^{3+}$ . Since there is oxygen depletion at the surface, these  $\text{Sb}^{3+}$  ions replace  $\text{Sn}^{2+}$  ions, thereby yielding increased electrical conductivity [59,60]. In agreement with the literature [54,56,57], the loss of electrical conductivity at high doping level (>10 at.%) observed in this study is believed to be caused by vaporization of Sb atoms during calcination at  $T = 873 \text{ K}$  (see Experimental Section). Calcination also leads to heterogeneities of chemical composition: X-EDS experiments evidenced that for doping of 15 at.%, some ATO grains featured a doping level of ca. 10 at.% in Sb, other grains were doped at 20 at.% ( $\text{Sb}/(\text{Sb} + \text{Sn}) = 14.2\% \pm 3.5\%$  in average), while for lower doping levels, the ATO composition was homogeneous. Since the specific surface area was also maximal at 10 at.% in Sb, the 10 at.% Sb-doped  $\text{SnO}_2$  support was chosen for Pt deposition and subsequent electrochemical characterization.

As shown by Fig. 1, the structure of the 10 at.% Sb-doped  $\text{SnO}_2$  aerogel is to some extent comparable to that of conventional carbon blacks used in PEMFC. Indeed, this support features spherical primary particles with size ca. 9 nm arranged in compact strings of beads. Mesoporosity and macroporosity are observed between the primary particles (Fig. 1b), which is highly commendable in terms of Pt utilization and effectiveness factor in the dynamic operating conditions of a PEMFC. The textural characteristics of the 10 at.% Sb-doped  $\text{SnO}_2$  support were obtained from nitrogen adsorption/desorption measurements performed at  $T = 77 \text{ K}$  with an automatic volumetric device ASAP 2020. A specific surface area of  $85 \text{ m}^2 \text{ g}^{-1}$ , a bimodal pore size distribution centered on 20 and 45 nm, and a negligible microporous volume ( $8 \times 10^{-3} \text{ cm}^3 \text{ g}^{-1}$ ) were found.

The XRD spectra recorded on the Sb-doped and undoped  $\text{SnO}_2$  supports are presented in Fig. 1d. The typical patterns of a polycrystalline rutile structure were observed independently of the degree of doping. No pattern characteristic of separated Sb phases ( $\text{Sb}$ ,  $\text{Sb}_2\text{O}_3$ ,  $\text{Sb}_2\text{O}_5$ ,  $\text{SbO}$  or  $\text{SbO}_2$ ) was detected, indicating that Sb atoms occupy Sn sites or insertion sites in the ATO aerogel.

### 3.2. Synthesis and characterization of the Pt/ATO and the Pt/C nanoparticles

Two synthesis routes were used to deposit Pt nanocrystallites onto the 10 at.% Sb-doped  $\text{SnO}_2$  aerogel: photoreduction or chemical reduction *via* a modified polyol method. For the samples prepared *via* the modified polyol route, a single colloidal solution served to platinize the ATO and the two reference supports (Vulcan XC72 and undoped  $\text{SnO}_2$ ). Therefore, a straightforward comparison of the catalytic performance of Pt nanocrystallites supported onto carbon,  $\text{SnO}_2$  (undoped) or ATO could be achieved. Preliminary experiments showed that a Pt mass fraction of 20 wt.% was optimal both on Pt specific surface area ( $S_{\text{Pt}}$ ) and specific ORR activity (SA) viewpoints (Fig. S1). The Pt weight percentage measured by atomic absorption spectroscopy (19 wt.% and 21 wt.% of Pt for the polyol and the photoreduction synthesis, respectively) was in agreement with the nominal value (20 wt.%) thereby indicating that both the photoreduction and the modified polyol methods were efficient. Table 2 summarizes the structural characteristics of the Pt/ATO and Pt/C electrocatalysts.

Fig. 2 displays TEM, STEM images, and X-EDS elemental maps of the Pt/ATO and the Pt/C samples. Homogeneously distributed Pt nanoparticles ca. 3 nm in size were observed for the Pt/C sample in TEM and STEM acquisition modes. However, because Pt nanocrystallites and ATO support could hardly be distinguished in conventional TEM (owing to the near-similar contrast between the two phases), the Pt particle size distribution was rebuilt from X-EDS elemental maps (see Fig. 2 and Fig. S4) for the Pt/ATO samples. The X-EDS elemental maps revealed a tendency to aggregation for the



**Table 1**

Textural and substructural properties of the ATO and the carbon supports investigated in this study. The BET surface area and porous volume for Vulcan XC-72 have been adapted from Table 12.1 of Ref. [61] with permission from John Wiley & Sons.

	SnO <sub>2</sub> (undoped)	5 at.% Sb-SnO <sub>2</sub>	10 at.% Sb-SnO <sub>2</sub>	15 at.% Sb-SnO <sub>2</sub>	Vulcan XC-72
Electrical conductivity (aerogel form for ATO)/S cm <sup>-1</sup>	$2 \times 10^{-5}$	0.1	0.1	0.01	4
BET surface area of the supports ( $S_{\text{BET}}$ )/m <sup>2</sup> g <sup>-1</sup>	81	56	85	42	252 (Ref. [61])
Total pore volume ( $V_{\text{p}}$ )/cm <sup>3</sup> g <sup>-1</sup>	0.31	0.21	0.27	0.13	0.63 (Ref. [61])
Micropore volume ( $V_{\text{p}}$ )/cm <sup>3</sup> g <sup>-1</sup>	$1.5 \times 10^{-2}$	$0.4 \times 10^{-2}$	$0.8 \times 10^{-2}$	$0.5 \times 10^{-2}$	$3.7 \times 10^{-2}$ (Ref. [61])
Diameter of the main pores/nm	15–20–40	20–30–45	20–45	20–45	20–35–350
Surface-weighted mean particle size <sup>a</sup> ( $d_{\text{S}}$ )/nm	$12 \pm 3$	$12 \pm 4$	$9 \pm 2$	$10 \pm 2$	$50 \pm 22$
Volume-weighted mean particle size <sup>a</sup> ( $d_{\text{V}}$ )/nm	$13 \pm 3$	$13 \pm 4$	$10 \pm 3$	$10 \pm 2$	$56 \pm 27$

<sup>a</sup> Determined from transmission electron micrographs.

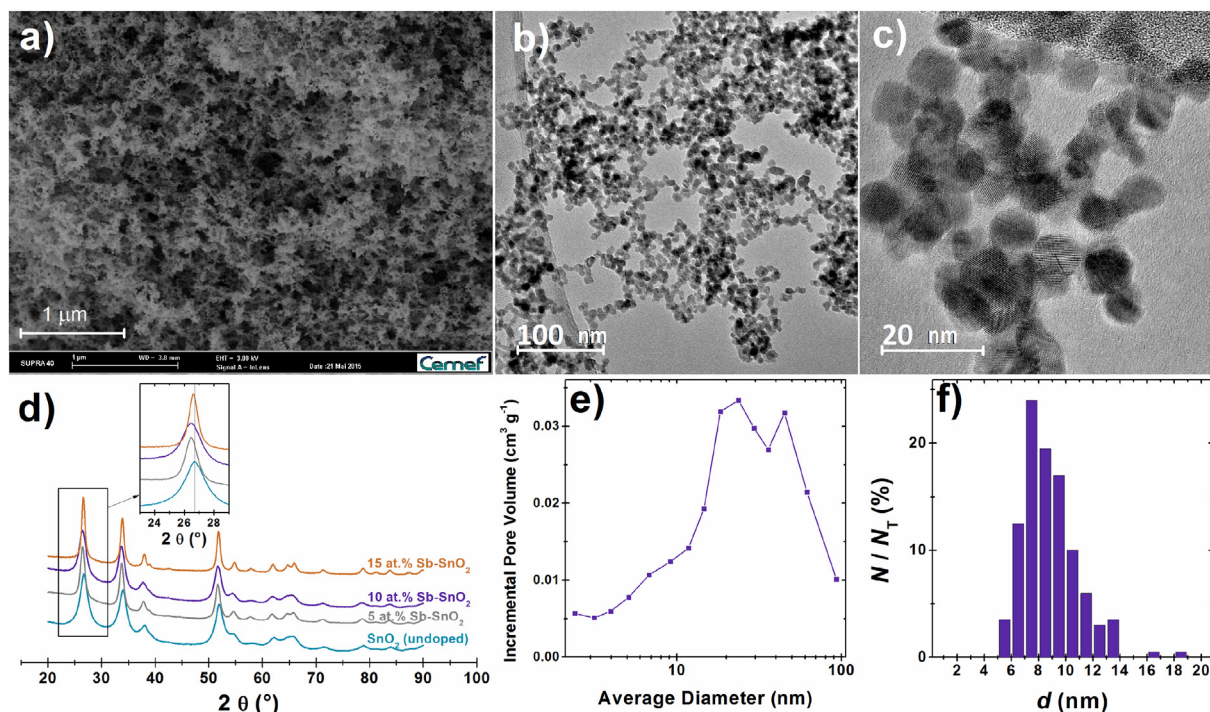


**Fig. 1.** Structural characteristics of the Sb-doped and undoped SnO<sub>2</sub> aerogels used in this study. (a) SEM, (b, c) TEM images, (e) pore size distribution and (f) particle size distribution of the 10 at.% Sb-doped SnO<sub>2</sub> support.  $N_T$  is the total number of counted particles ( $N_T \approx 200$ ). (d) X-ray diffractograms of the synthesized Sb-doped and the undoped SnO<sub>2</sub> aerogels.

**Table 2**

Structural properties of the Pt/ATO and Pt/C electrocatalysts used in this study.

	Pt/C–polyol	Pt/ATO–polyol	Pt/ATO–photoreduction
Pt weight fraction/wt.%	20	19	21
$d_{\text{S}}^b$ /nm	$2.5 \pm 0.5$	$2.7 \pm 0.4$	$3.3 \pm 0.7$
$d_{\text{V}}^b$ /nm	$2.6 \pm 0.6$	$2.7 \pm 0.4$	$3.5 \pm 0.7$
$d_{\text{XRD}}^b$ /nm	$2.4 \pm 0.2$	$3.4 \pm 0.2$	$3.9 \pm 0.2$

<sup>b</sup> Determined from STEM images and X-EDS elemental maps by counting only the isolated Pt nanoparticles.

Pt nanoparticles deposited on ATO, this trend being emphasized for the photoreduction procedure. The increase in the degree of aggregated Pt nanoparticles is not specific to the ATO supports but occurs when the specific surface area of the support is  $<100 \text{ m}^2 \text{ g}^{-1}$  (see similar observations on Pt/reinforced graphite in Ref. [8]). Interestingly, it did not reflect in the XRD spectra (nearly constant mean crystallite size was obtained from the fit of the Pt(111) peak using the Debye–Scherrer equation), suggesting that the Pt aggregates were composed of several adjacent nanocrystallites.

### 3.3. Electrochemical characterization of the Pt/ATO and the Pt/C electrocatalysts

Fig. 3 displays cyclic voltammograms (CVs) for the Pt/ATO, the Pt/SnO<sub>2</sub> (undoped) and the reference Pt/C electrocatalysts obtained via the photoreduction and the modified polyol routes. For the sake of comparison, the CVs of the bare Sb-SnO<sub>2</sub> aerogel and the SnO<sub>2</sub> (undoped) aerogel supports are provided in Fig. 3b. According to previous findings of the group on Pt/H<sub>x</sub>WO<sub>4</sub> [34] and of Fabri et al. [62] on Pt/Ir<sub>0.8</sub>Ti<sub>0.2</sub>O<sub>2</sub> and Pt/Sb-doped SnO<sub>2</sub>, CO<sub>ads</sub>

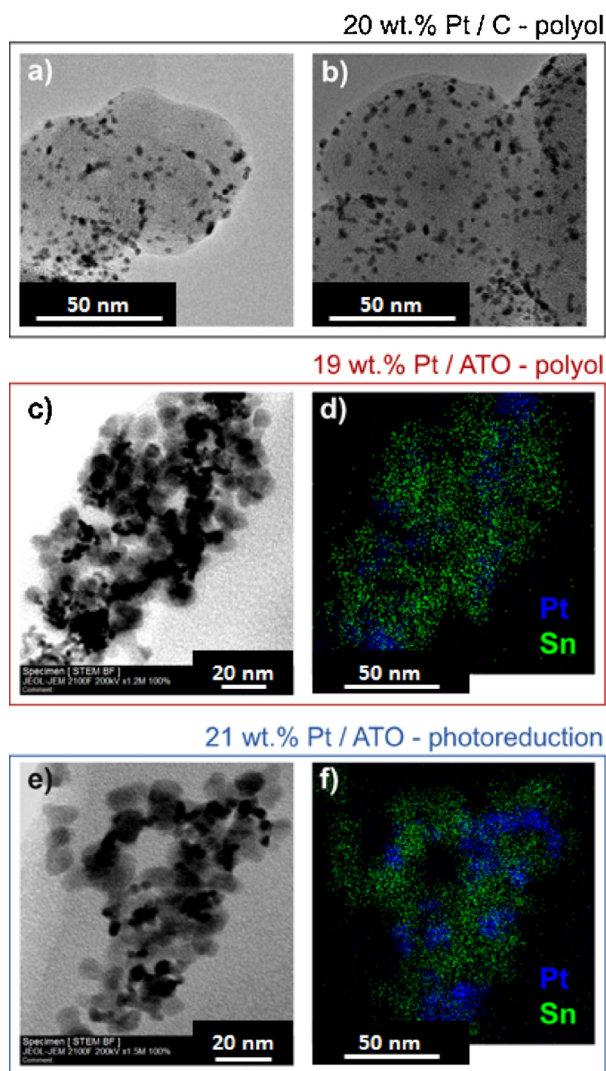


**Fig. 2.** TEM and STEM images, and X-EDS elemental maps of the synthesized electrocatalysts (Pt nanoparticles deposited on Vulcan XC72 or on 10 at.% Sb-SnO<sub>2</sub> aerogel)—the Pt nanoparticles are the dark spots in the TEM-STEM images (a, b, c and e) and the blue areas in the X-EDS elemental maps (d and f).

stripping is not a reliable technique to measure the real surface area of Pt nanoparticles supported on metal oxides. In consequence, the coulometry required to adsorb/desorb a monolayer of underpotentially-deposited hydrogen ( $H_{\text{upd}}$ ) was used to determine the real surface area of all the samples.

Independently of the nature of the support, the CVs featured the adsorption/desorption of  $H_{\text{upd}}$  between 0.05 and 0.40 V vs. the RHE, surface oxide formation at  $0.75 < E < 1.2$  V vs. RHE, and surface oxide reduction at  $0.45 < E < 1.2$  V vs. RHE. A marked difference between the synthesized materials was the presence of a redox peak in the CV of the Pt/ATO sample (oxidation peak at  $E \sim 0.75$  V vs. RHE; reduction peak at  $E \sim 0.69$  V vs. RHE), and its absence from the CV of Pt/C. This pair of peaks is controversially rationalized in the literature: it is associated to the dissolution of the doping element (Sb), [27] to the Sn(II)/Sn(IV) redox couple [63] or to the dissolution/redeposition of Sn atoms from the SnO<sub>2</sub> lattice [31]. In the present study, this pair of redox peaks was observed in the 1st scan of the CV measured on the bare SnO<sub>2</sub> (undoped) support and the Pt/SnO<sub>2</sub> (undoped) electrocatalysts while it was not visible on the 15th scan represented in Fig. 3, therefore suggesting that Sn is involved. Note also that this pair of peaks was independent on the synthesis procedure, as shown by its presence in the CV of

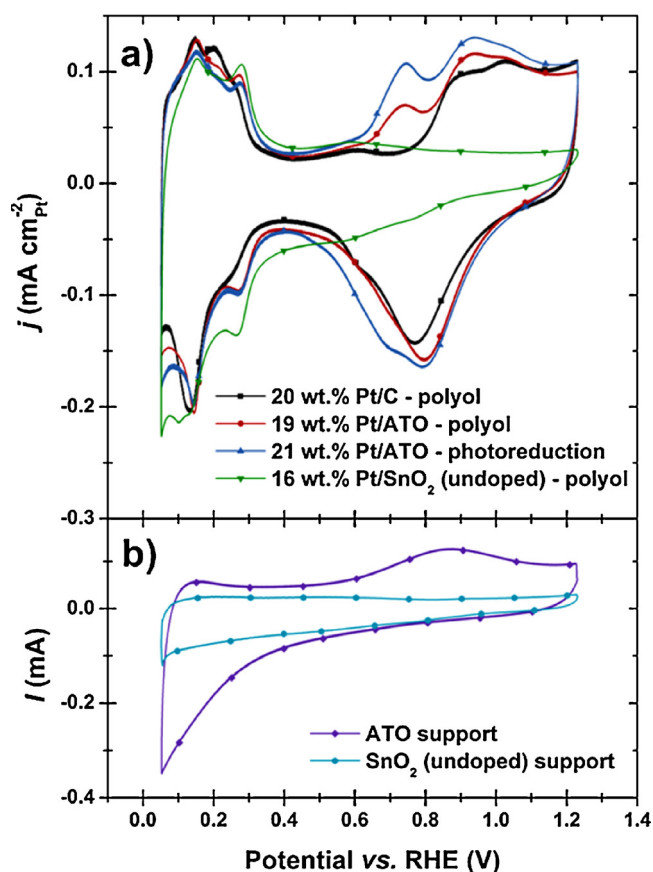


**Fig. 3.** Electrochemical characterization of the materials synthesized in this study. Cyclic voltammograms in supporting electrolyte for (a) the electrocatalysts and (b) the bare supports. For the Pt/C, Pt/ATO and Pt/SnO<sub>2</sub> samples, a Pt loading of  $L_{\text{Pt}} = 60 \mu\text{g}_{\text{Pt}} \text{cm}_{\text{geo}}^{-2}$  revealed optimal both on Pt specific surface area, specific ORR activity, and durability (the specific ORR activity should be measurable after the AST) aspects (Fig. S2). The current was normalized to the real Pt surface area determined from the  $H_{\text{upd}}$  coulometry in (a), whereas the (non-normalized) current is displayed in (b).  $\nu = 100 \text{ mV s}^{-1}$ ,  $T = 330 \text{ K}$ —Electrolyte: 0.1 M H<sub>2</sub>SO<sub>4</sub>.

the Pt/ATO sample prepared by photoreduction or modified polyol route.

Smaller ECSA and Pt specific surface area were measured on Pt/ATO relative to the reference Pt/C (Fig. 4).

Since these two samples were prepared from the same colloidal solution, and since the electrochemical measurements were realized with the same Pt loading, the decrease of Pt specific surface area suggests that either (i) Pt nanoparticles are agglomerated on ATO, (ii) poisoned by the ATO support or that (iii) partially reduced SnO<sub>x</sub> species (or Sb atoms) back-spillover from the ATO support onto the Pt nanoparticles. The latter scenario would go in line with former observations that nanometer-sized noble metals (Pt, Pd, Ir, Rh) supported onto reducible metal-oxides (WO<sub>3</sub>, TiO<sub>2</sub>, NbO<sub>2</sub>) become partially or fully encapsulated (the so-called “decoration effect” associated with strong metal support interactions, SMSI) [34,64–67].

The electrocatalytic activity for the oxygen reduction reaction (ORR) of the Pt/ATO and Pt/C samples synthesized *via* the polyol and the photoreduction route was also evaluated from linear sweep voltammograms. To be as representative as possible from real PEMFC operating conditions [46], the measurements were realized at  $T = 330 \text{ K}$  (the reference electrode used in this work prohibited temperatures greater than 333 K). Fig. 4b shows linear sweep voltammograms recorded in O<sub>2</sub>-saturated 0.1 M H<sub>2</sub>SO<sub>4</sub> on Pt/C, Pt/ATO, and Pt/SnO<sub>2</sub>. A strong dependence of the diffusion-limited current on the electrical conductivity of the support was observed

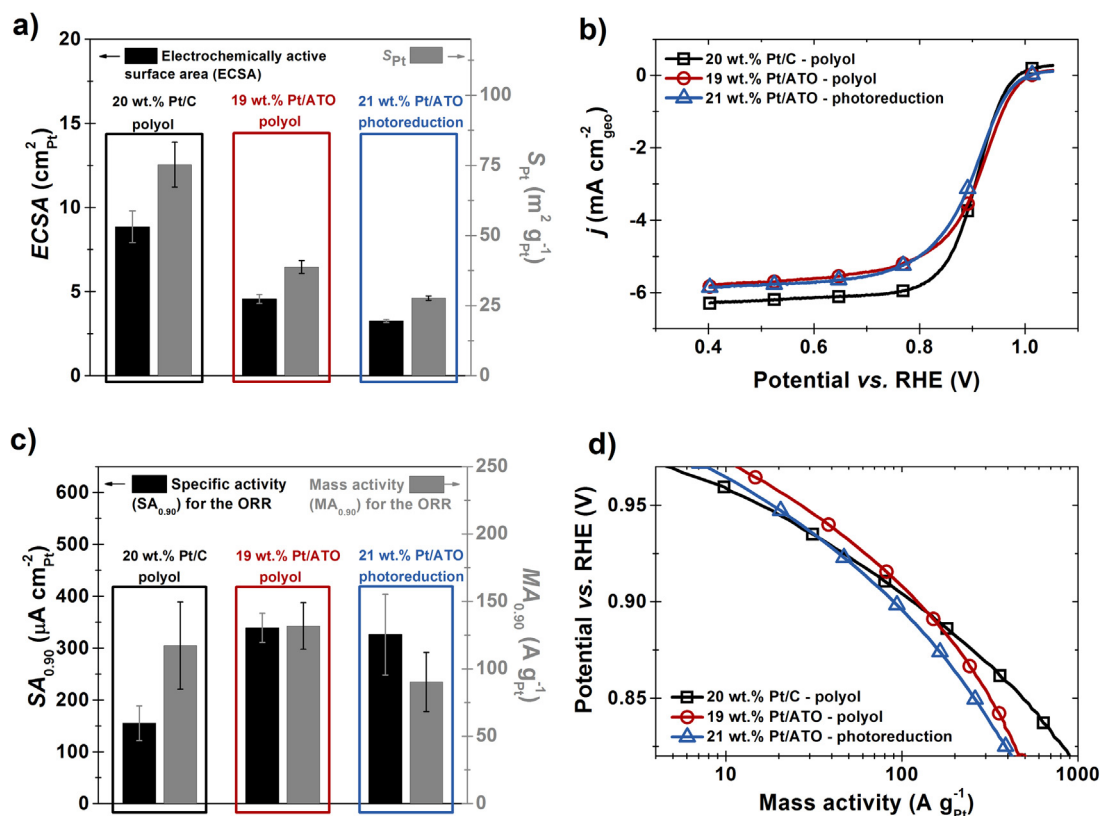


**Fig. 4.** Electrocatalytic properties of the Pt/C and the Pt/ATO samples. a) Electrochemically active surface area (ECSA) and Pt specific surface area ( $S_{Pt}$ ). The ECSA was determined by using the coulometry required to adsorb and desorb  $H_{upd}$  from the Pt nanoparticles. b) Linear sweep voltammograms recorded on the Pt/ATO and Pt/C samples recorded at  $\nu = 5 \text{ mV s}^{-1}$  in  $\text{O}_2$  saturated electrolyte. c) Specific activity ( $SA_{0.90}$ ) and mass activity ( $MA_{0.90}$ ) for the ORR determined at  $E = 0.90 \text{ V}$  vs. RHE. d) Tafel plots of Ohmic and mass-transport corrected linear sweep voltammograms displayed in b).  $T = 330 \text{ K}$  – Electrolyte:  $0.1 \text{ M H}_2\text{SO}_4$ – $L_{Pt} = 60 \mu\text{g}_{Pt} \text{ cm}_{geo}^{-2}$  – The error bars are the standard deviations of at least three independent measurements.

(Pt/C > Pt/ATO > Pt/SnO<sub>2</sub> in absolute value). This result can easily be rationalized by considering electrical conductivity of the supports. Hence, when the electrical conductivity of the supports is lowered, some Pt nanoparticles are not in electrical contact and the glassy carbon disk is no longer geometrically covered. For the same Pt loading, all Pt nanoparticles supported on Vulcan XC72 are in electrical contact with the glassy carbon disk, and hence the diffusion limited current is reached. As shown by Fig. S5, this scenario was confirmed quantitatively.

The kinetic current for the ORR was determined from the linear sweep voltammograms, after correction from Ohmic drop and oxygen transport in solution, and expressed under the form of specific activity or mass activity at  $E = 0.90 \text{ V}$  vs. RHE ( $SA_{0.90}$  and  $MA_{0.90}$ , respectively). Larger  $SA_{0.90}$  values were found for Pt/ATO relative to Pt/C; however, due to their lower Pt specific surface area, the materials featured similar  $MA_{0.90}$  values. Here again, the interest of using a unique colloidal suspension to prepare the Pt/C and a Pt/ATO samples is obvious: indeed, as both samples feature identical mean Pt crystallite size (see Table 2), the observed difference in specific activity cannot be ascribed to a “crystallite size effect”. Note also that two methods (modified polyol and photoreduction) were used to synthesize Pt/ATO materials: the similar catalytic trend obtained via the two routes suggests that the enhanced values of  $SA_{0.90}$  observed on the Pt/ATO samples result from a synergy between the Pt nanoparticles and the ATO support. This hypothesis is further supported by the literature: a two-times-high specific activity for the ORR was also found on Pt/ATO relative to a Pt/C by Yin *et al.* [68], and on Pt nanoparticles supported on SnO<sub>2</sub> films without preferential orientation by Rabis *et al.* [69].

### 3.4. Stability of the Pt/ATO and the Pt/C electrocatalysts in model PEMFC startup/shutdown conditions

To gain insights into the long-term catalytic performance of the Pt/ATO samples, accelerated stress tests (AST) mimicking high-potential excursions experienced by a PEMFC cathode during start/stop or fuel starvation events were performed. The ASTs consisted of modulating the electrode potential with a square wave between 1.0 and 1.5 V vs. RHE with a holding time of 3 s at each voltage (protocol recommended by the Fuel Cell Commercialization Conference of Japan – FCCJ – see Experimental Section). Fig. 5 displays the CVs monitored after 5,000 and 10,000 potential cycles on Pt/ATO and on the reference Pt/C.

On Pt/C, nearly 100% of the ECSA was lost after 10,000 potential cycles as reflected by the large variation of the charge density in the  $H_{upd}$  region. The variation was much smaller on the Pt/ATO sample, and this provides evidence that ATO supports are more robust during model PEMFC startup/shutdown conditions. Note however that the double layer capacitance increased markedly on the aged ATO supports, therefore suggesting some physico-chemical degradations (that do not alter the Pt ECSA).

Another interesting finding emerged from the CVs in the potential region  $0.6 < E < 0.90 \text{ V}$  vs. RHE, where Pt surface oxides are formed and reduced (Fig. 5). On Pt/C, the surface oxide formation/reduction features were strongly depreciated after the AST (as for the  $H_{upd}$  region), suggesting that the Pt nanoparticles had massively detached from the carbon support during the AST. Other experimental evidences of the corrosion of the carbon support were the increase of the intensity of the redox peaks in the potential range  $0.5 < E < 0.8 \text{ V}$  vs. RHE (ascribed to electron transfer on/from



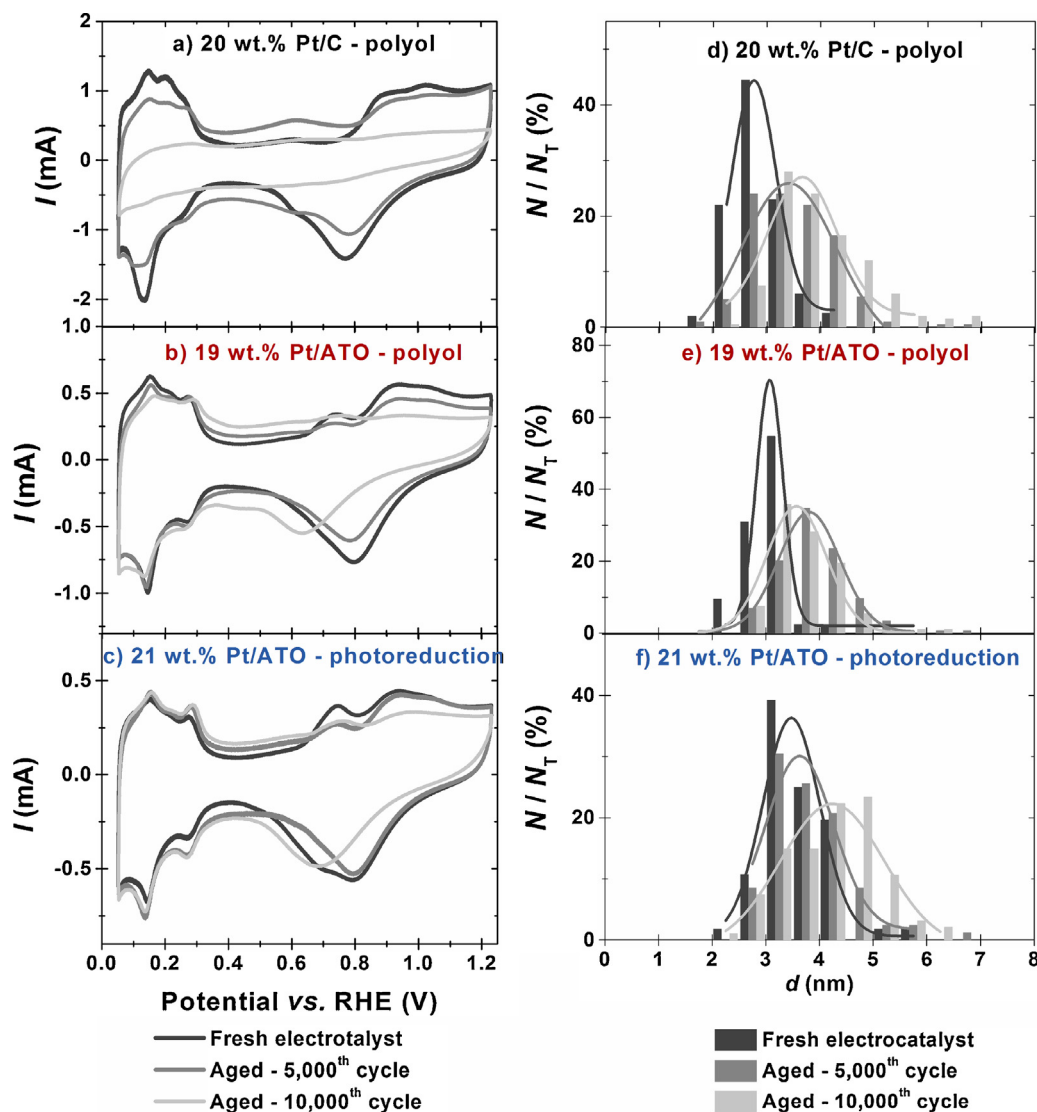


**Fig. 5.** Representative cyclic voltammograms for the Pt/ATO and the reference Pt/C electrocatalysts before/after AST (a, b and c) and associated particle size distributions (d, e and f).  $T = 330\text{ K}$ —Electrolyte:  $0.1\text{ M H}_2\text{SO}_4$ — $\nu = 100\text{ mV s}^{-1}$ — $L_{\text{Pt}} = 60\text{ }\mu\text{g}_{\text{Pt}}\text{ cm}_{\text{geo}}^{-2}$ .  $N_T$  stands for the total number of counted particles ( $N_T = 200$  for the Pt/C sample and  $50 < N_T < 100$  for the Pt/ATO samples). To avoid the deleterious effect of intermediate characterizations [48], a single electrode was utilized for each AST (i.e. the 10 k cycled electrode is different from the 5 k cycled electrode). All measurements were performed at least two times.

hydroquinone/quinone) and the increase of the pseudocapacitance of the electrode during ageing [70]. As shown by the positive shift of the potential of the Pt surface oxide reduction peak in electrochemical measurements [71] and by TEM images (Fig. 5), the size of the Pt nanocrystallites that did not detach from the carbon support increased markedly. Similar changes of the Pt particle size distribution were noticed on ATO (Fig. 5e and f). However, strikingly, the potential of the Pt surface oxide reduction peak did not shift towards positive potential values after 10,000 potential cycles for Pt/ATO. Also, the ratio of the charge required to form surface oxides to that required to desorb  $\text{H}_{\text{upd}}$  was severely depreciated on the aged Pt/ATO samples: this suggests increased irreversibility of the formation/reduction of surface oxides on Pt/ATO.

In agreement with these changes in electrochemical properties, the specific activity for the ORR increased on the reference Pt/C electrocatalyst (beneficial effect of the increase of the mean crystallite size), and only slightly decreased on the Pt/ATO samples during the first 5,000 potential cycles. The benefit of supporting Pt nanoparticles on ATO progressively disappeared after 5,000 potential cycles

(Fig. 6). As described below, these variations may be rationalized by the loss of Sb atoms from the ATO support during the AST.

### 3.5. Change of the degree of doping in the surface/near-surface region

Table 3 displays the variation of the Sb content measured by XPS (a surface sensitive technique) and by X-EDS (a bulk technique for nanomaterials) on the bare and the platinized ATO supports during the AST. Note that the  $\text{Sb}/(\text{Sb} + \text{Sn})$  ratio is different on the bare ATO support ( $11.6 \pm 0.7\%$ ) and the fresh Pt/ATO samples (ca. 8–10 at.%). As observed by the authors, this reflects different Sb and Sn X-EDS intensities when Pt is present/absent in the samples, and must not be ascribed to Sb atoms being washed from the ATO support during the Pt deposition process.

For all samples, two kinetic regimes were observed: the variation of the  $\text{Sb}/(\text{Sb} + \text{Sn})$  ratio was fast during the first 5,000 potential cycles and slower later on. We also noticed that the change in the Sb content was stronger at the surface of the Pt/ATO electrocatalysts than in their bulk (see the variations of the Sb content measured



**Table 3**

Sb/(Sb+Sn) at.% ratio measured by X-EDS and XPS for un-platinized and platinized ATO supports before and after the AST [3 s at 1 V vs. RHE–3 s at 1.5 V vs. RHE].

	Bare ATO	Pt/ATO–polyol		Pt/ATO–photoreduction	
	X-EDS	X-EDS	XPS	X-EDS	XPS
Fresh	11.6 ± 0.7%	8.2 ± 0.8%	7.9 ± 0.8%	9.9 ± 1.1%	12.9 ± 1.3%
After 5,000 potential cycles	8.5 ± 1.0%	6.1 ± 0.9%		7.0 ± 0.6%	
After 10,000 potential cycles	8.5 ± 1.1%	5.6 ± 0.6%	3.7 ± 0.4%	7.0 ± 0.4%	5.2 ± 0.5%

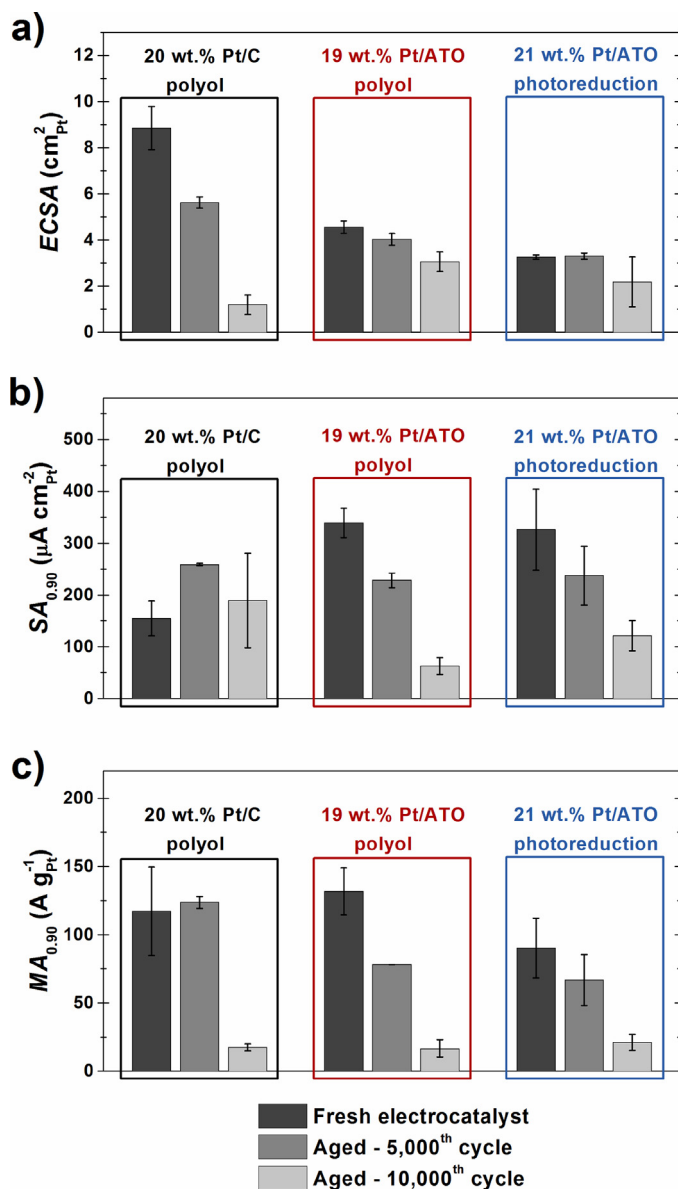


**Fig. 6.** Variations of (a) the electrochemically active surface area, (b) the specific activity and (c) the mass activity for the ORR determined at  $E = 0.90$  V vs. RHE during a model startup/shutdown protocol (3 s at 1.0 V vs. RHE–3 s at 1.5 V vs. RHE). The specific activity for the ORR was normalized by the ECSA calculated after the durability test, whereas the mass activity was calculated based on the initial mass of Pt deposited onto the electrode—Electrolyte: 0.1 M  $\text{H}_2\text{SO}_4$ — $T = 330$  K— $v = 100$  mV s<sup>-1</sup>— $L_{\text{Pt}} = 60$  μg<sub>Pt</sub> cm<sub>geo</sub><sup>-2</sup>. Each value is the average of at least two independent experiments.

by XPS and X-EDS). These results strongly suggest the formation of a core@shell nanostructure where the surface is Sb-poor and the bulk features a composition close to that of the raw material, in agreement with former observations of Fabbri *et al.* [27].

Based on these results, the changes in ORR activity of the Pt/ATO electrocatalysts during ageing are easy to rationalize. Indeed, it is

well-established in literature that the electrical conductivity of a metal oxide is sensitive to the molecules present in the surrounding atmosphere [72,73]. In particular, in the presence of oxygen species, the conductivity of undoped-SnO<sub>2</sub> [72–74] or doped-SnO<sub>2</sub> [75] (with Nb leading to a low initial conductivity) is strongly depreciated. A highly-doped ATO support has a sufficiently high electrical conductivity and is not sensitive to the band bending involved by the adsorption of oxygenated species. However, when the surface concentration of Sb atoms decreases, as it is the case for the aged ATO supports, the support possesses a lower conductivity and is thus more sensitive to the adsorption of oxygenated species. Convincing experimental evidences of this scenario are visible in Figs. 5 and 3: the loss of Sb atoms firstly renders the formation/reduction of Pt surface oxides more irreversible (negative shift of the Pt oxide reduction peak in Fig. 5), and ultimately impossible (see the CV of Pt/SnO<sub>2</sub> (undoped) in Fig. 3). In consequence, despite their better resistance to corrosion, meeting sustainably the electron-conductivity criterion remains hardly challenging on ATO aerogels, and further research efforts should be focused on maintaining the Sb surface concentration constant.

#### 4. Conclusion

Using a sol-gel route in acidic media, Sb-doped SnO<sub>2</sub> metal aerogels with high BET area, high electron conductivity and better corrosion-resistance than Vulcan XC72 in the 1.0 <  $E$  < 1.5 V vs. RHE potential range were synthesized and characterized. A Sb concentration of 10 at.% was found to be optimal in terms of electrical conductivity and specific surface area. The 10 at.% doped SnO<sub>2</sub> aerogel featured a specific surface area of 85 m<sup>2</sup> g<sup>-1</sup>, a bimodal pore size distribution centered on 25 and 45 nm, and a negligible microporous volume ( $8 \times 10^{-3}$  cm<sup>3</sup> g<sup>-1</sup>). Two reference materials, Pt/Vulcan XC72 and Pt/undoped SnO<sub>2</sub>, were synthesized using the same Pt colloidal suspension, which allowed a straightforward comparison of the electrocatalytic activity for the ORR and the stability of Pt nanoparticles on the different supports. A 2-fold enhancement in specific activity for the ORR was measured on Pt/ATO over the reference Pt/Vulcan XC72. The ATO support was more resistant to corrosion during an AST mimicking startup/shutdown of a PEMFC device. However, the AST also revealed some limitations of ATO supports: Sb atoms were lost during ageing, yielding ultimately a support featuring a Sb-poor shell covering a core with a Sb content close to the nominal. The depletion of Sb atoms from the ATO surface restricted the capacity of Pt nanoparticles to exchange electrons with their support, as evidenced by the attenuated Pt surface oxide formation/reduction features, and the decreased catalytic activity for the ORR monitored post-ageing tests.

#### Acknowledgment

This work was performed within the framework of the Centre of Excellence of Multifunctional Architected Materials “CEMAM” n° AN-10-LABX-44-01 funded by the “Investments for the Future” program. The authors acknowledge financial support from the French National Research Agency through the SURICAT project (grant

number ANR-12-PRGE-007) as well as Capenergies and Tenerrdis. MC thanks the French IUF for its support.

## Appendix A. Supplementary data

Supplementary data associated with this article can be found, in the online version, at <http://dx.doi.org/10.1016/j.apcatb.2016.08.010>.

## References

- [1] L. Dubau, L. Castanheira, F. Maillard, M. Chatenet, O. Lottin, G. Maranzana, J. Dillet, A. Lamibrac, J.C. Perrin, E. Moukheiber, A. Elkaddouri, G. De Moor, C. Bas, L. Flandin, N. Caqué, Wiley Interdiscip. Rev. Energy Environ. 3 (6) (2014) 540–560.
- [2] L. Dubau, L. Castanheira, G. Berthomé, F. Maillard, Electrochim. Acta 110 (2013) 273–281.
- [3] E. Guilminot, A. Corcella, M. Chatenet, F. Maillard, F. Charlot, G. Berthomé, C. Jojoiu, J.Y. Sanchez, E. Rossinot, E. Claude, J. Electrochem. Soc. 154 (11) (2007) B1106–B1114.
- [4] E. Guilminot, A. Corcella, F. Charlot, F. Maillard, M. Chatenet, J. Electrochem. Soc. 154 (1) (2007) B96–B105.
- [5] L. Dubau, J. Durst, F. Maillard, M. Chatenet, J. André, E. Rossinot, Fuel Cells 12 (2) (2012) 188–198.
- [6] Z. Zhao, L. Dubau, F. Maillard, J. Power Sources 217 (2012) 449–458.
- [7] L. Castanheira, L. Dubau, M. Mermoux, G. Berthomé, N. Caqué, E. Rossinot, M. Chatenet, F. Maillard, ACS Catal. 4 (7) (2014) 2258–2267.
- [8] L. Castanheira, W.O. Silva, F.H.B. Lima, A. Crisci, L. Dubau, F. Maillard, ACS Catal. (2015) 2184–2194.
- [9] M. Pourbaix, Atlas d'équilibres électrochimiques, Gauthier-Villars, 1963.
- [10] S. Maass, F. Finsterwalder, G. Frank, R. Hartmann, C. Merten, J. Power Sources 176 (2) (2008) 444–451.
- [11] F. Maillard, A. Bonnefont, F. Micoud, Electrochem. Commun. 13 (10) (2011) 1109–1111.
- [12] N. Linse, L. Gubler, G.G. Scherer, A. Wokaun, Electrochim. Acta 56 (22) (2011) 7541–7549.
- [13] L.M. Roen, C.H. Paik, T.D. Jarvi, Electrochem. Solid State Lett. 7 (1) (2004) A19–A22.
- [14] L. Dubau, M. Lopez-Haro, L. Castanheira, J. Durst, M. Chatenet, P. Bayle-Guillemaud, L. Guétaz, N. Caqué, E. Rossinot, F. Maillard, Appl. Catal. B Environ. 142–143 (2013) 801–808.
- [15] A. Taniguchi, T. Akita, K. Yasuda, Y. Miyazaki, J. Power Sources 130 (1–2) (2004) 42–49.
- [16] J. Durst, A. Lamibrac, F. Charlot, J. Dillet, L.F. Castanheira, G. Maranzana, L. Dubau, F. Maillard, M. Chatenet, O. Lottin, Appl. Catal. B Environ. 138–139 (0) (2013) 416–426.
- [17] J. Dillet, D. Spornjak, A. Lamibrac, G. Maranzana, R. Mukundan, J. Fairweather, S. Didierjean, R.L. Borup, O. Lottin, J. Power Sources 250 (2014) 68–79.
- [18] Y. Ishigami, K. Takada, H. Yano, J. Inukai, M. Uchida, Y. Nagumo, T. Hyakutake, H. Nishide, M. Watanabe, J. Power Sources 196 (6) (2011) 3003–3008.
- [19] C.A. Reiser, L. Bregoli, T.W. Patterson, J.S. Yi, J.D.L. Yang, M.L. Perry, T.D. Jarvi, Electrochem. Solid State Lett. 8 (6) (2005) A273–A276.
- [20] Z.Y. Liu, B.K. Brady, R.N. Carter, B. Litteer, M. Budinski, J.K. Hyun, D.A. Muller, J. Electrochem. Soc. 155 (10) (2008) B979–B984.
- [21] A. Lamibrac, G. Maranzana, O. Lottin, J. Dillet, J. Mainka, S. Didierjean, A. Thomas, C. Moyne, J. Power Sources 196 (22) (2011) 9451–9458.
- [22] C. Galeano, J.C. Meier, V. Peinecke, H. Bongard, I. Katsounaros, A.A. Topalov, A. Lu, K.J.J. Mayrhofer, F. Schüth, J. Am. Chem. Soc. 134 (50) (2012) 20457–20465.
- [23] S. Cavaliere, S. Subianto, L. Chevallier, D.J. Jones, J. Rozière, Chem. Commun. 47 (24) (2011) 6834–6836.
- [24] S. Cavaliere, S. Subianto, I. Savych, M. Tillard, D.J. Jones, J. Rozière, J. Phys. Chem. C 117 (36) (2013) 18298–18307.
- [25] I. Cerri, T. Nagami, J. Davies, C. Mormiche, A. Vecoven, B. Hayden, Int. J. Hydrogen Energy 38 (1) (2013) 640–645.
- [26] L. Chevallier, A. Bauer, S. Cavaliere, R. Hui, J. Rozière, D.J. Jones, ACS Appl. Mater. Interfaces 4 (3) (2012) 1752–1759.
- [27] E. Fabbri, A. Rabis, R. Kötz, T.J. Schmidt, Phys. Chem. Chem. Phys. 16 (27) (2014) 13672–13681.
- [28] E. Fabbri, A. Pătru, A. Rabis, R. Kötz, T.J. Schmidt, Chimia (Aarau) 68 (4) (2014) 217–220.
- [29] M. Gustavsson, H. Ekstrom, R. Hanarp, L. Eurenus, G. Lindbergh, E. Olsson, B. Kasemo, J. Power Sources 163 (2) (2007) 671–678.
- [30] T. Ioroi, H. Senoh, S.I. Yamazaki, Z. Siroma, N. Fujiwara, K. Yasuda, J. Electrochem. Soc. 155 (4) (2008) B321–B326.
- [31] K. Kakinuma, Y. Chino, Y. Senoo, M. Uchida, T. Kamino, H. Uchida, S. Deki, M. Watanabe, Electrochim. Acta 110 (2013) 316–324.
- [32] K. Kakinuma, I.T. Kim, Y. Senoo, H. Yano, M. Watanabe, M. Uchida, ACS Appl. Mater. Interfaces 6 (24) (2014) 22138–22145.
- [33] D. Konopka, B. Kiefer, Y.-B. Jiang, T. Ward, P. Atanassov, J. Electrochem. Soc. 158 (7) (2011) B804–B813.
- [34] F. Micoud, F. Maillard, A. Bonnefont, N. Job, M. Chatenet, Phys. Chem. Chem. Phys. 12 (2010) 1182–1193.
- [35] F. Micoud, F. Maillard, A. Gourgau, M. Chatenet, Electrochem. Commun. 11 (2009) 651–654.
- [36] K.W. Park, K.S. Seol, Electrochem. Commun. 9 (9) (2007) 2256–2260.
- [37] K. Sasaki, F. Takasaki, Z. Noda, S. Hayashi, Y. Shiratori, K. Ito, ECS Trans. 33 (2010) 473–482.
- [38] F. Takasaki, S. Matsue, Y. Takabatake, Z. Noda, A. Hayashi, Y. Shiratori, K. Ito, K. Sasaki, J. Electrochem. Soc. 158 (10) (2011) B1270–B1275.
- [39] Y. Takabatake, Z. Noda, S.M. Lyth, A. Hayashi, K. Sasaki, Int. J. Hydrogen Energy 39 (10) (2014) 5074–5082.
- [40] Y. Senoo, K. Taniguchi, K. Kakinuma, M. Uchida, H. Uchida, S. Deki, M. Watanabe, Electrochem. Commun. 51 (2015) 37–40.
- [41] M. Batzill, U. Diebold, Prog. Surf. Sci. 79 (2–4) (2005) 47–154.
- [42] I. Savych, J. Bernard D'Arbigny, S. Subianto, S. Cavaliere, D.J. Jones, J. Rozière, J. Power Sources 257 (2014) 147–155.
- [43] A. Masao, S. Noda, F. Takasaki, K. Ito, K. Sasaki, Electrochem. Solid State Lett. 12 (9) (2009) B119–B122.
- [44] R.G. Egdel, J. Rebane, T.J. Walker, D.S.L. Law, Phys. Rev. B: Condens. Matter Mater. Phys. 59 (3) (1999) 1792–1799.
- [45] D. Riassetto, C. Holtzinger, M. Messaoud, S. Briche, G. Berthomé, F. Roussel, L. Rapenne, M. Langlet, J. Photochem. Photobiol. A Chem. 202 (2–3) (2009) 214–220.
- [46] L. Dubau, F. Maillard, Electrochem. Commun. 63 (2016) 65–69.
- [47] A. Ohma, K. Shinohara, A. Iiyama, T. Yoshida, A. Daimaru, 220th ECS Meeting. ECS (2011) 775–784.
- [48] L. Castanheira, L. Dubau, F. Maillard, Electroanalysis 5 (2) (2014) 125–135.
- [49] D. Briggs, M.P. Seah, Practical Surface Analysis, Auger and X-ray Photoelectron Spectroscopy; Practical Surface Analysis, Wiley, 1990.
- [50] C.D. Wagner, G.E. Muilenberg, Handbook of X-ray Photoelectron Spectroscopy: A Reference Book of Standard Data for Use in X-ray Photoelectron Spectroscopy; Physical Electronics Division, Perkin-Elmer Corp., 1979.
- [51] C. Vittoz, P. Bossis, F. Lefebvre, J.C. Joud, J. Adhes. Sci. Technol. 13 (9) (1999) 1045–1061.
- [52] S. Tanuma, C.J. Powell, D.R. Penn, Surf. Interface Anal. 21 (3) (1994) 165–176.
- [53] J.H. Scofield, J. Electron Spectrosc. Relat. Phenom. 8 (2) (1976) 129–137.
- [54] Y. Cross, D.R. Pyke, J. Catal. 58 (1) (1979) 61–67.
- [55] Y. Boudeville, F. Figueras, M. Forissier, J.L. Portefaix, J.C. Vedrine, J. Catal. 58 (1) (1979) 52–60.
- [56] D. Dobler, S. Oswald, J. Werner, W. Arabczyk, G. Behr, K. Wetzig, Chem. Phys. 286 (2–3) (2003) 375–383.
- [57] S. Oswald, G. Behr, D. Dobler, J. Werner, K. Wetzig, W. Arabczyk, Anal. Bioanal. Chem. 378 (2) (2004) 411–415.
- [58] D. Szczuko, J. Werner, S. Oswald, G. Behr, K. Wetzig, Appl. Surf. Sci. 179 (1–4) (2001) 301–306.
- [59] D.R. Leite, I.O. Mazali, E.C. Aguiar, W.C. Las, M. Cilense, J. Mater. Sci. 41 (19) (2006) 6256–6259.
- [60] P.A. Cox, R.G. Egdel, C. Harding, W.R. Patterson, P.J. Tavener, Surf. Sci. 123 (2–3) (1982) 179–203.
- [61] F. Maillard, P. Simonov, E.R. Savinova, in: P. Serp, J.L. Figueiredo (Eds.), Carbon Materials for Catalysis, vol. 5, John Wiley & Sons, Inc., New York, 2009, pp. 429–480.
- [62] T. Binninger, E. Fabbri, R. Kötz, T.J. Schmidt, J. Electrochem. Soc. 161 (3) (2014) H121–H128.
- [63] M. Nakada, A. Ishihara, S. Mitsushima, N. Kamiya, K. Ota, Electrochem. Solid State Lett. 10 (1) (2007) F1.
- [64] Q. Fu, T. Wagner, Surf. Sci. Rep. 62 (11) (2007) 431–498.
- [65] U. Diebold, Surf. Sci. Rep. 48 (5–8) (2003) 53–229.
- [66] Q. Fu, T. Wagner, S. Olliges, H.D. Carstanjen, J. Phys. Chem. B 109 (2) (2005) 944–951.
- [67] V.A. de la P. O'shea, M.C.A. Galván, A.E.P. Prats, J.M. Campos-Martin, J.L.G. Fierro, Chem. Commun. (Camb.) 47 (25) (2011) 7131–7133.
- [68] M. Yin, J. Xu, Q. Li, J.O. Jensen, Y. Huang, L.N. Cleemann, N.J. Bjerrum, W. Xing, Appl. Catal. B Environ. 144 (1) (2014) 112–120.
- [69] A. Rabis, D. Kramer, E. Fabbri, M. Worsdale, R. Kötz, T.J. Schmidt, J. Phys. Chem. C 118 (21) (2014) 11292–11302.
- [70] K. Kinoshita, Carbon, Electrochemical and Physicochemical Properties, John Wiley & Sons, New York, 1988.
- [71] F. Maillard, S. Pronkin, E.R. Savinova, Influence of size on the electrocatalytic activities of supported metal nanoparticles in fuel cells related reactions, in: W. Vielstich, H.A. Gasteiger, H. Yokokawa (Eds.), Handbook of Fuel Cells Vol. 5 “Advances in Electrocatalysis, Materials, Diagnostics and Durability”, John Wiley & Sons, Inc.: New York, 2009, pp. 91–111.
- [72] M.E. Franke, T.J. Koplin, U. Simon, Small 2 (1) (2006) 36–50.
- [73] C. Wang, L. Yin, L. Zhang, D. Xiang, R. Gao, Sensors 10 (3) (2010) 2088–2106.
- [74] J.F. Boyle, K.A. Jones, J. Electron. Mater. 6 (6) (1977) 717–733.
- [75] Y. Senoo, K. Kakinuma, M. Uchida, H. Uchida, S. Deki, M. Watanabe, RSC Adv. 4 (61) (2014) 32180–32188.